

Dynamics of Laterally Propagating Flames in X-ray Bursts. II. Realistic Burning & Rotation

ALICE HARPOLE,¹ NICOLE FORD,² KIRAN EIDEN,¹ MICHAEL ZINGALE,^{1,3} DONALD WILLCOX,²
YURI CAVECCHI,⁴ AND MAX P. KATZ⁵

¹*Dept. of Physics and Astronomy, Stony Brook University, Stony Brook, NY 11794-3800*

²*Lawrence Berkeley National Laboratory, Berkeley, CA*

³*Center for Computational Astrophysics, Flatiron Institute, New York, NY 10010*

⁴*Mathematical Sciences and STAG Research Centre, University of Southampton, SO17 1BJ*

⁵*NVIDIA Corp*

ABSTRACT

We continue to investigate laterally propagating flames in XRBs using fully compressible hydrodynamics simulations. In the current study we relax the approximations used previously and explore the effect of rotation rate and the thermal structure of the neutron star on the flame. We find that higher temperature atmospheres lead to faster flames and observe acceleration of the flame front as it propagates through the atmosphere. All of the software used for these simulations is freely available.

Keywords: X-ray bursts (1814), Nucleosynthesis (1131), Hydrodynamical simulations (767), Hydrodynamics (1963), Neutron stars (1108), Open source software (1866), Computational methods (1965)

1. INTRODUCTION

Considerable evidence suggests that ignition in an X-ray burst starts in a localized region and then spreads across the surface of the neutron star (Bhattacharyya & Strohmayer 2007; Chakraborty & Bhattacharyya 2014). We continue our study of flame spreading through fully compressible hydrodynamics simulations of the flame. Building on our previous paper (Eiden et al. 2020), we relax the approximations we made previously (artificially boosting the speed of the flame in order to reduce the computational cost) and explore how the flame properties depend on rotation rate and the thermal structure of the neutron star. This new set of realistic simulations is possible because of the work done to offload our simulation code, *Castro* (Almgren et al. 2020), to GPUs, where it runs significantly faster.

We investigate the effect of rotation rate on the flame. With the exception of Altamirano et al. (2010), most observations of XRBs come from sources with rotation rates of 200-600Hz (Bilous & Watts 2019; Galloway et al. 2020). There are a number of factors that could explain this lack of observations below 200 Hz. It could be that there is some physical process which inhibits the flame ignition and/or spread at lower rotation rates. It could be that burst oscillations at lower rotation rates are smaller in amplitude and

check
whether this
is true for
XRBs or just
burst
oscillations

therefore more difficult to detect. It could be that it's not got anything to do with the flame at all, but that neutron stars in accreting low mass X-ray binaries rarely have rotation rates below 200 Hz .

look into
this?

Previous studies have found that rotation can have a significant affect on the flame's propagation. As the rotation rate increases, the Coriolis force whips the spreading flame up into a hurricane-like structure (Spitkovsky et al. 2002; Cavecchi et al. 2013). The stronger Coriolis force leads to greater confinement of the hot accreted matter, leading to easier ignition of the flame (Cavecchi et al. 2015).

The temperature structure of the accreted fuel layer can also affect the flame propagation. Timmes (2000) showed that laminar helium flames have higher speeds when moving into hotter upstream fuel. It is known that crustal heating is stronger at lower accretion rates and weaker at higher accretion rates, due to the effect of neutrino losses (Cumming et al. 2006; Johnston et al. 2019). In our models, we keep the crust at a constant temperature, so by increasing this temperature we can effectively increase the crustal heating and/or mimic the effects of higher accretion rates. A shallow heating mechanism of as yet unknown origin has been found necessary to reproduce observed properties of XRBs (Deibel et al. 2015; Turlione et al. 2015; Keek & Heger 2017).

In the following sections, we conduct a series of simulations at various rotation rates and temperatures to investigate their effects on the flame. We find that at lower rotation rates, the flame itself becomes harder to ignite. At higher rotation rates, nuclear burning is enhanced and the flame propagates more quickly. At high temperatures, burning is greatly enhanced and the flame accelerates as it propagates. We discuss the implications that this may have for burst physics and observations.

2. NUMERICAL APPROACH

mz

We use the Castro hydrodynamics code (Almgren et al. 2010; Almgren et al. 2020) and the simulation framework introduced in Eiden et al. (2020). The current simulations are all performed in a two-dimensional axisymmetric geometry. For these axisymmetric simulations, we add a missing geometric source terms from Bernard-Champmartin et al. (2012) that captures the effects of the divergence of the flux operating on the azimuthal unit vector. This term is a small correction, but was missing from our earlier simulations. The simulations framework initializes a fuel layer in hydrostatic equilibrium, laterally blending a hot model on the left side of the domain (the coordinate origin) and a cool model on the right. The initial temperature gradient between the hot and cool models drives a laterally propagating flame through the cool fuel. In our original set of calculations, we artificially boosted the flame speed by adjusting the conductivity and reaction rate to produce a flame moving 5–10 \times faster than the nominal laminar flame speed. We also used high rotation rates to reduce the lateral lengthscale at which the Coriolis force balances the lateral flame spreading. For the current simulations, we no longer boost the flame speed—the true conductivities (taken from Timmes 2000) and reaction rates are used. We continue to use a 13-isotope α -chain to describe the helium burning. The port of Castro to GPUs (Katz et al. 2020) enables us to run these simulations without the previous approximations, while continuing to resolve the burning front.

The initial model is set up in the same fashion as described in Eiden et al. (2020). In particular, we create a “hot” and “cool” hydrostatic model representing the ash and fuel states and blend the two models laterally to create a hot region near the origin of coordinates and a smooth transition to the cooler region at larger radii. The cool initial characterized by 3 temperatures: T_{star} is the isothermal temperature of the underlying neutron star, T_{hi} is the temperature at the base of the fuel layer, and T_{lo} is the minimum temperature of the atmosphere—the atmosphere structure is isentropic as it falls from T_{hi} down to T_{lo} . For the hot model, we replace T_{hi} with $T_{\text{hi}} + \delta T$. In the calculations presented here, we explore the structure of the initial models by varying these parameters. All models have the same peak temperature in the hot model, $T_{\text{star}} + \delta T$.

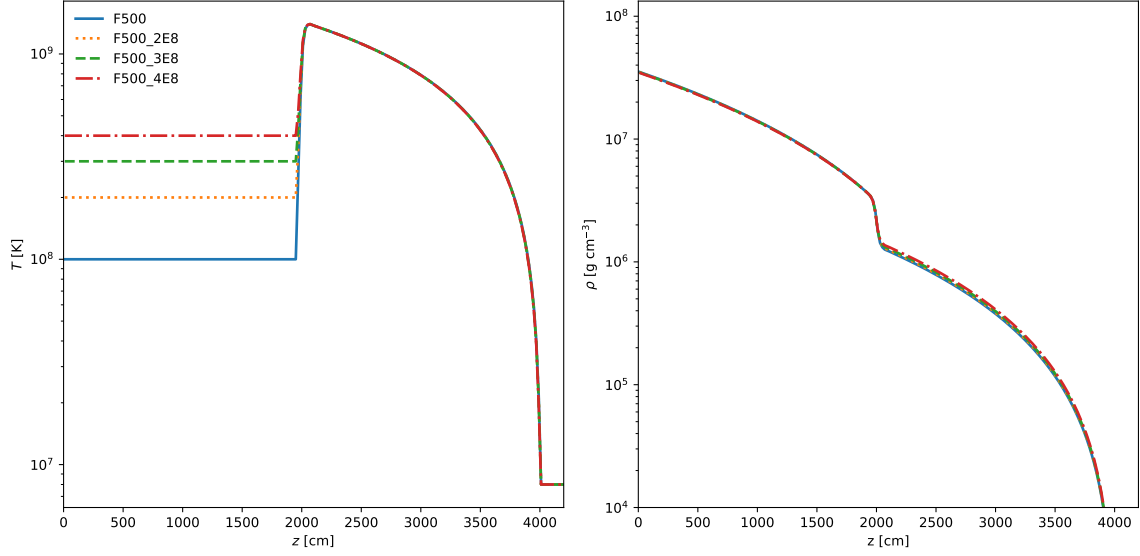


Figure 1. Initial temperature and density structure vs. height in the “hot” state.

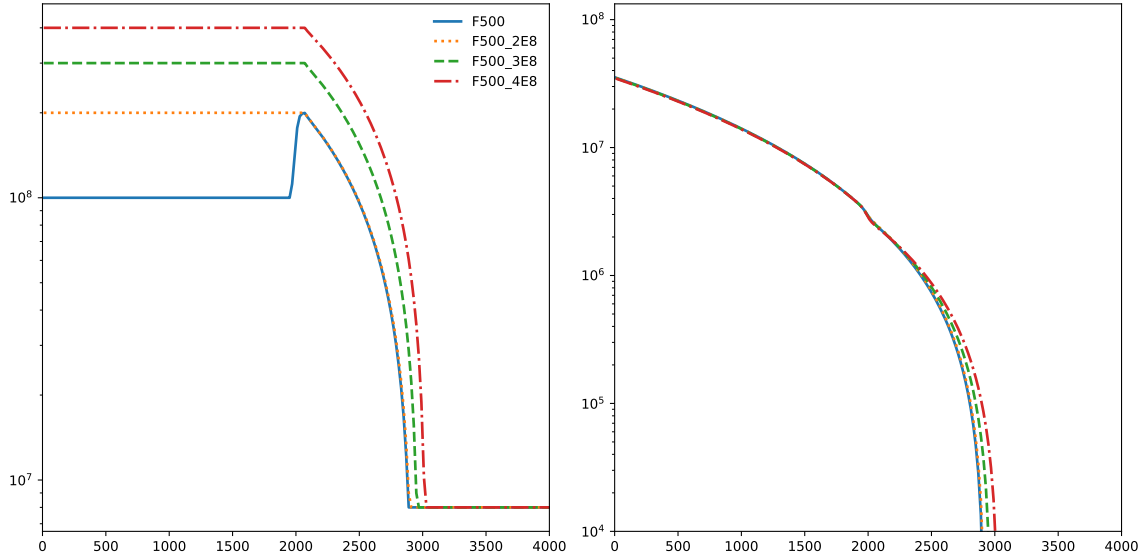


Figure 2. Initial temperature and density structure vs. height in the “cool” state.

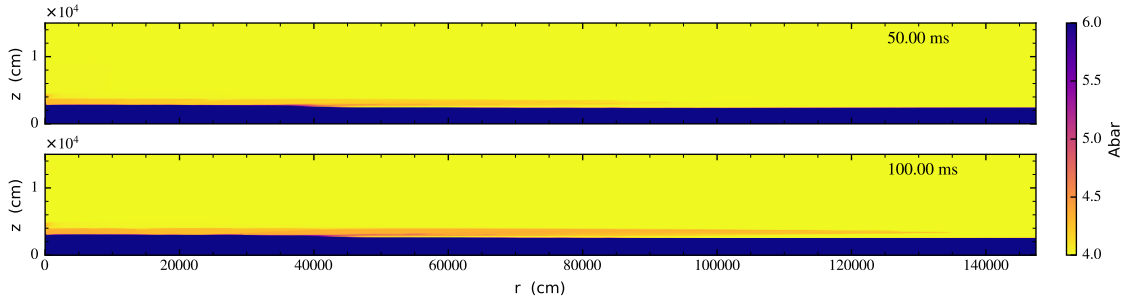
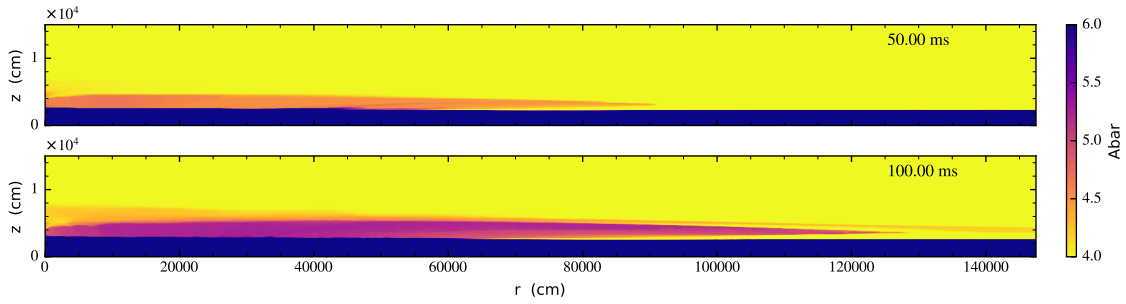
For the current simulations, we explore a variety of initial rotation rate and temperature conditions for the flame. The main parameters describing the models are provided in Table 1. Figure 1 shows the temperature and density structure for our hot models and figure 2 shows the temperature and density structure for the cool models.

3. SIMULATIONS AND RESULTS

We present six simulations in total, summarized in Table 1. These simulations encompass three different rotation rates: 250 Hz, 500 Hz, and 1000 Hz, and for the 500 Hz run, four different temperature profiles. In the following subsections, we look at how the flame properties depend on the model parameters. All simulations are run in a domain of 1.8432×10^5 cm \times 3.072×10^4 cm with a coarse grid of 1152×192

Table 1. Rotation rate and temperature properties of the simulations.

run	Rotation Rate (Hz)	δT (K)	T_{hi} (K)	T_{star} (K)	T_{lo} (K)
F1000	1000	1.2×10^9	2×10^8	10^8	8×10^6
F500	500	1.2×10^9	2×10^8	10^8	8×10^6
F500_2E8	500	1.2×10^9	2×10^8	2×10^8	8×10^6
F500_3E8	500	1.1×10^9	3×10^8	3×10^8	8×10^6
F500_4E8	500	10^9	4×10^8	4×10^8	8×10^6
F250	250	1.2×10^9	2×10^8	10^8	8×10^6

**Figure 3.** Time series of F500 showing \bar{A} .**Figure 4.** Time series of F1000 showing \bar{A} .

zones and two levels of refinement (the first a jump by a factor of four and the second a jump by a factor of two finer). This gives a fine-grid resolution of 20 cm. The entire atmosphere is refined in these simulations, with the refinement tagging on all zones with $\rho > 2.5 \times 10^4 \text{ g cm}^{-3}$.

3.1. Effect of Rotation Rate on Flame Structure

We run three models (F250, F500, and F1000) with the same initial model but differing rotation rates.

The F500 and F1000 runs both qualitatively resemble the flame structure in Eiden et al. (2020) — a laterally propagating flame that is lifted off of the bottom of the fuel layer — but they differ in their burning structures. Figures 3 and 4 show time series of the mean molecular weight (\bar{A}) for the F500 and F1000 runs. Compared to those in Eiden et al. (2020), ashes behind the flame do not reach as high atomic weights.

update both
the abar
figures to
only show 50
ms and 100
ms
snapshots
update both
the abar
figures to
only show 50
ms and 100
ms
snapshots

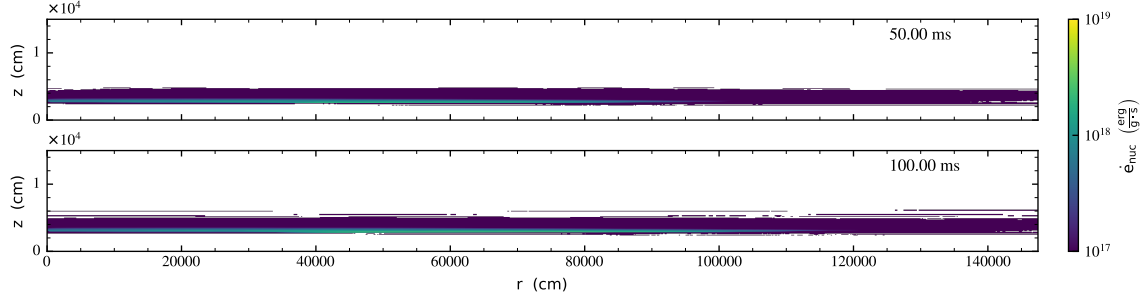


Figure 5. Time series of F500 showing \dot{e}_{nuc} .

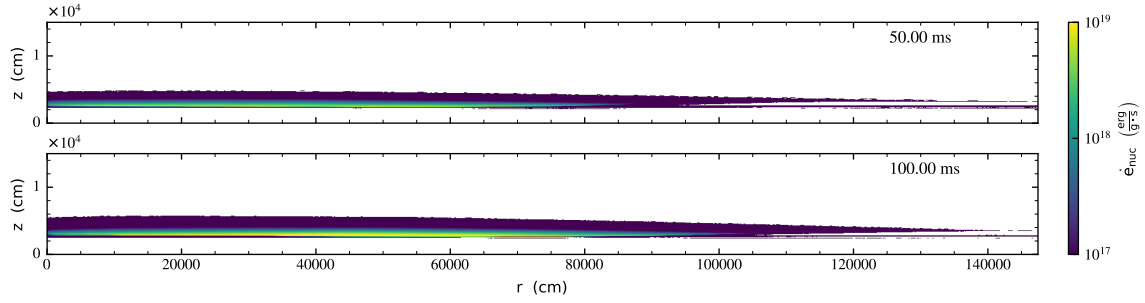


Figure 6. Time series of F1000 showing \dot{e}_{nuc} .

This is not surprising, since those early runs boosted the reaction rates. Comparing these two new runs, the burning is much more evolved for the higher rotation rate, and the ash is actually able to move ahead of the flame front (visible in the Figure 4 100 ms snapshot). We believe that this is because the increased rotation confines the initial perturbation and subsequent expansion from the burning better, allowing the reactions to progress further. In contrast to F500 and F1000, the lowest rotation run — F250 — failed to ignite. The lack of ignition for F250 also aligns with the reasoning given above, with the lower rotation in this case potentially leading to insufficient confinement of the burning. In this scenario, another source of confinement (e.g. magnetic fields) would need to take over at lower rotation rates to allow a burst to occur, at least for our current initial model.

Burning in the F500 and F1000 runs is concentrated in a dense region with circular motion. Figure 7 compares the horizontal x -velocity u , density ρ and the nuclear energy generation rate \dot{e}_{nuc} for F250, F500, and F1000. Most of the burning for each of the simulations occurs in a high density region $\rho > 3 \times 10^5 \text{ g/cm}^3$. The fluid in this dense, high energy generation region undergoes vortical motion, shown in the Figure 8 phase plots comparing u , v and \dot{e}_{nuc} . From the previous plots (see: streamlines?), this most likely corresponds to the leading edge of the flame where fresh fuel is being entrained. This feature is not developed in the 250 Hz flame; it could potentially develop at later times, or the flame could just fizzle out.

The mean molecular weight \bar{A} within each of our simulations seems to grow along defined tracks confined to certain temperatures T , as shown in the Figure 9 phase plots. We believe that the tracks in the plot correspond to reaction pathways in the reaction network. Comparing Figure 9 to Eiden et al. (2020), these tracks are much more neat and clearly defined. The "messiness" of the tracks may be dependent on how mixed the flame interior is — since these new simulations are un-boosted, they may be inherently less

NF: which plots?

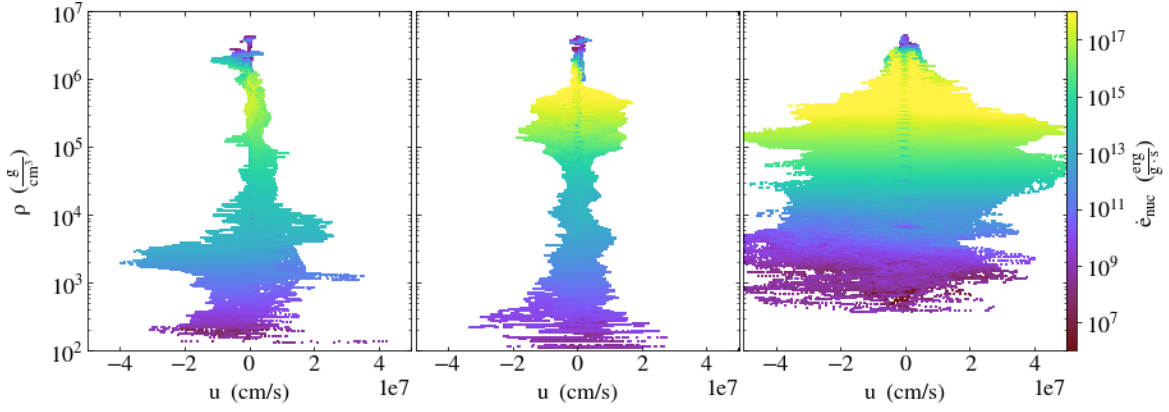


Figure 7. Phase plot of the horizontal x -velocity u , density ρ and the nuclear energy generation rate \dot{e}_{nuc} for the 250, 500 and 1000 Hz runs.

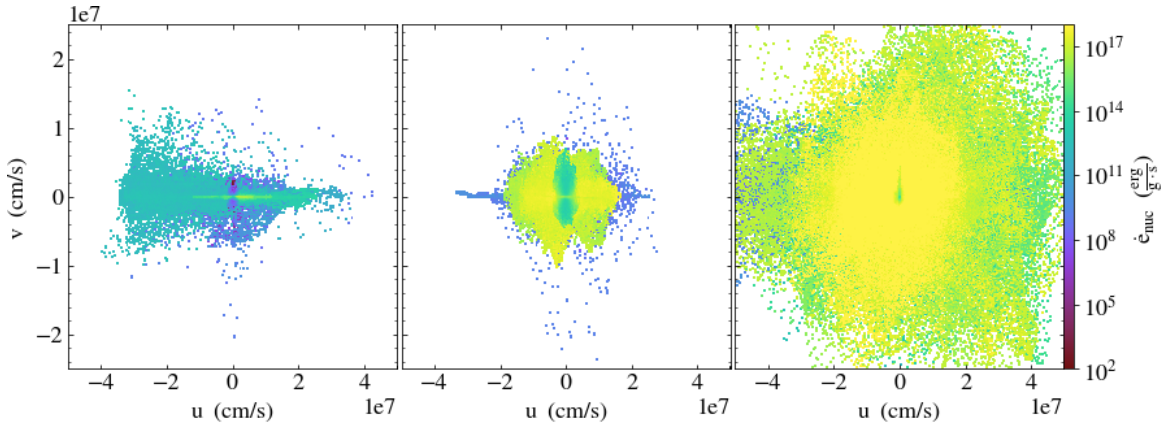


Figure 8. Phase plot of the horizontal x -velocity u , vertical y -velocity v and the nuclear energy generation rate \dot{e}_{nuc} for the 250, 500 and 1000 Hz runs.

mixed than those in Eiden et al. (2020). F1000 aligns with this interpretation: its \bar{A} tracks are somewhat disrupted compared to the slower rotation runs, possibly due to the more vigorous mixing of the vortex at the flame front. Comparing the different runs, we also see that as the rotation rate increases, so does the peak temperature. This makes sense if higher rotation leads to a more concentrated, intense vortex near the flame front. It also agrees with our earlier interpretation of the enhanced burning seen in Figure 4 for F1000. The disruption of reaction pathways with higher rotation rates and mixed flames may have interesting consequences; if the reactions are disrupted enough, it is possible that the burning could be snuffed out. This can occur in combustion scenarios when the turbulent vortices become so small they penetrate the reaction zone and completely disrupt the burning.

MZ: lateral profiles of X vs distance behind the flame; vertical profiles of the atmosphere behind the flame—how does it compare to isentropic?

what is the composition on the photosphere across the flame

shape of flame, amount of mixing (e.g. it looks like slower rotation rates have less mixed flames as the hurricane is less strong.)

Don: look at ratio of e_{nuc} to e ?

3.2. Effect of Rotation Rate on Flame Propagation

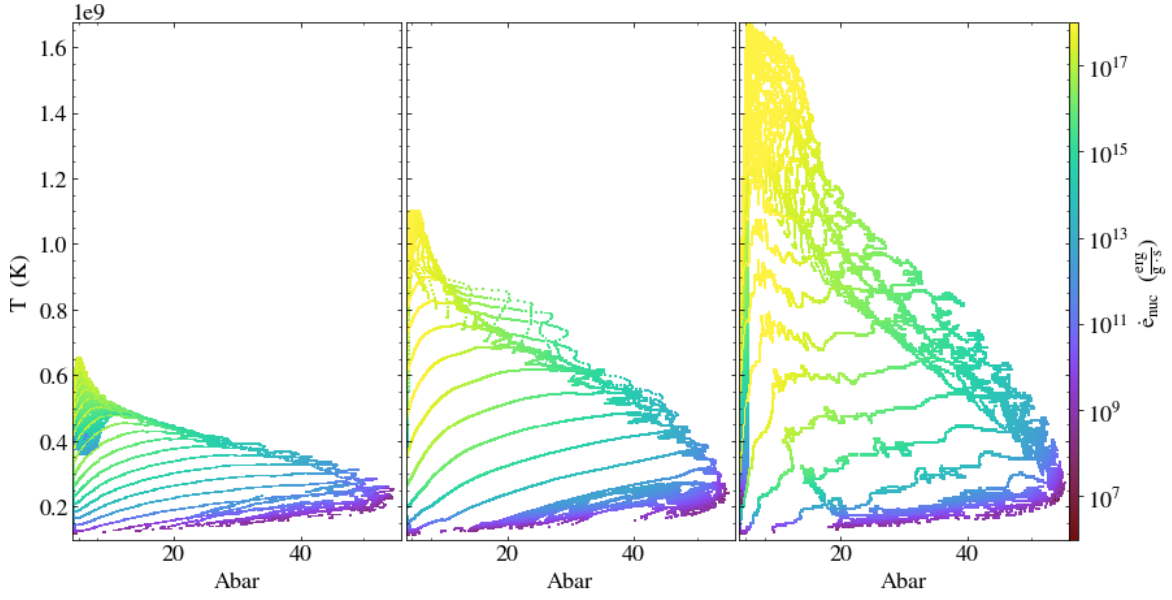


Figure 9. Phase plot of the mean molecular weight \bar{A} , temperature T and the nuclear energy generation rate $\dot{\epsilon}_{\text{nuc}}$ for the 250, 500 and 1000 Hz runs.

For the purpose of measuring the flame propagation speed and acceleration, we track the position of each of our flames as a function of time. We define the position in terms of a particular energy generation rate ($\dot{\epsilon}_{\text{nuc}}$) value, as we did in Eiden et al. (2020). To recapitulate: we first reduce the 2D $\dot{\epsilon}_{\text{nuc}}$ data for each simulation run to a set of 1D radial profiles by averaging over the vertical coordinate. After averaging, we take our reference $\dot{\epsilon}_{\text{nuc}}$ value to be some fraction of the global $\dot{\epsilon}_{\text{nuc}}$ maximum across all of these profiles. Since the flames in our simulations propagate rightward, we then search the region of each profile to the right of the local $\dot{\epsilon}_{\text{nuc}}$ maximum for the point where the $\dot{\epsilon}_{\text{nuc}}$ first drops below this reference value. This point gives us the location of our flame front.

In Eiden et al. (2020), we used 0.1% of the global $\dot{\epsilon}_{\text{nuc}}$ maximum for our reference value. For the high temperature unboosted flames, however, we found that the $\dot{\epsilon}_{\text{nuc}}$ profiles failed to reach that small a value across the domain at most times, which prevented us from getting reliable position measurements. We therefore use 1% of the global $\dot{\epsilon}_{\text{nuc}}$ maximum in this paper rather than 0.1%. This is still sufficiently small that our measurements are not overly sensitive to turbulence and other local fluid motions (the issue with simply tracking the local maximum), but allows us to avoid the pitfall encountered by the 0.1% metric.

Figure 10 gives position vs. time for the F500 and F1000 runs (blue and orange, respectively) to show the dependence on rotation rate. As some of the hotter 500 Hz runs exhibit significant accelerations, we fit a quadratic curve to each set of data for times $t \gtrsim 0.02$ s and calculate the acceleration and initial velocity from the fit parameters. These results are given in Table 2.

We found in Eiden et al. (2020) that the flame speed s obeys:

$$s \propto L_R (\dot{\epsilon})^{\frac{1}{2}} \propto \frac{(\dot{\epsilon})^{\frac{1}{2}}}{\Omega} \quad (1)$$

where $\dot{\epsilon}$ is the specific energy generation rate and L_R is the Rossby length. This was consistent with the results of Cavecchi et al. (2013), who noted that the flame speeds in their simulations scaled with the Rossby length. As seen in Figure 10, there is no obvious inverse scaling of the flame speed with rotation rate in this set of runs. We observed earlier, however, that nuclear reactions progress more quickly at the higher rotation

How is the acceleration calculated for this table? I.e. Specifically, at what time / over what time window is it calculated? NF-T will update the error estimates

Table 2. Flame speed and acceleration values measured for each simulation. s_0 is the speed at $t = 0$. The initial flame velocities and accelerations are derived from a quadratic least-squares fit to each of the datasets for times $t \gtrsim 0.02$ s.

run	s_0 (cm s $^{-1}$)	a (cm s $^{-2}$)
F1000	$(3.41 \pm 0.01) \times 10^5$	$(-1.03 \pm 0.13) \times 10^5$
F500	$(3.08 \pm 0.01) \times 10^5$	$(5.41 \pm 0.19) \times 10^5$
F500_2E8	$(3.76 \pm 0.02) \times 10^5$	$(1.74 \pm 0.17) \times 10^5$
F500_3E8	$(5.29 \pm 0.10) \times 10^5$	$(3.57 \pm 0.02) \times 10^7$

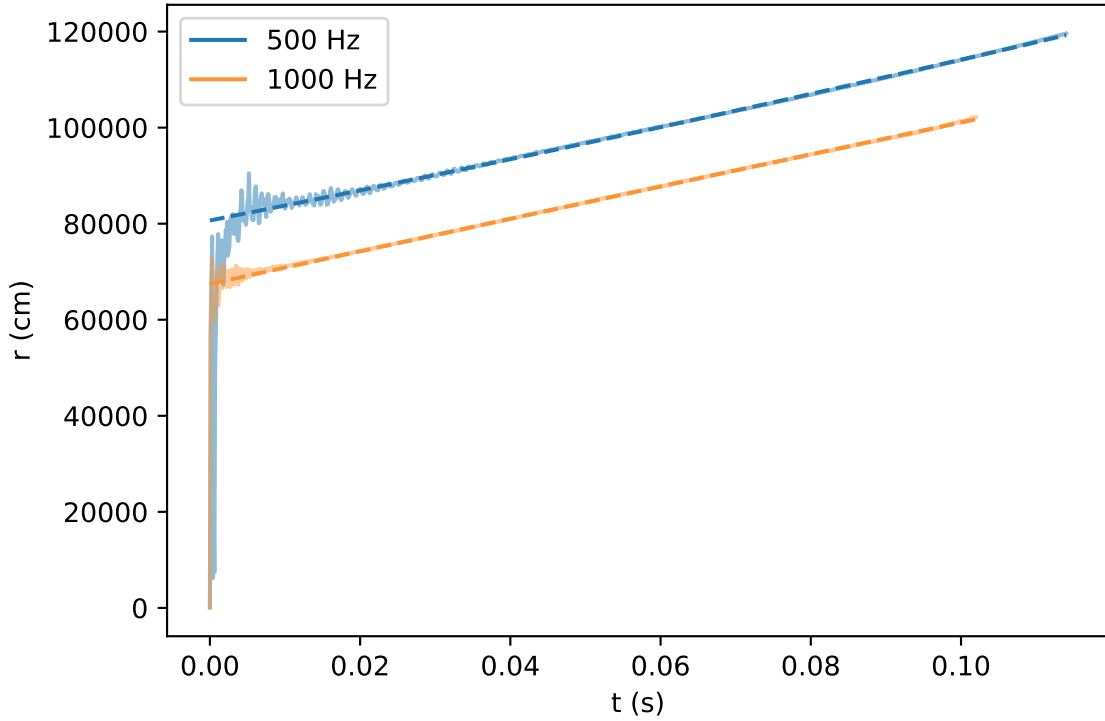


Figure 10. Flame front position vs. time for the standard (10^8 K) 500 Hz and 1000 Hz runs. The dashed lines show quadratic least-squares fits to the data for $t \gtrsim 0.02$ s.

rate. This results in a higher \dot{e}_{nuc} — up to four to six times higher near the burning front after the flame ignites — which may counteract the reduction in flame speed from the increased Coriolis confinement. The initial position of F1000 does appear to be reduced compared to the lower rotation F500 run. From Equation 1, increasing the rotation rate from 500 Hz to 1000 Hz should decrease L_R by a factor of two, and the initial position of the flame should be reduced by a similar factor (again, due to greater confinement from the Coriolis force). L_R is not, however, a perfect metric for the flame lengthscale. The scaling described in Equation 1 seems to be more accurate at higher rotation rates (1000 Hz and up), based on Eiden et al. (2020). We also observe that F500 accelerates faster than F1000, which appears to experience a small deceleration

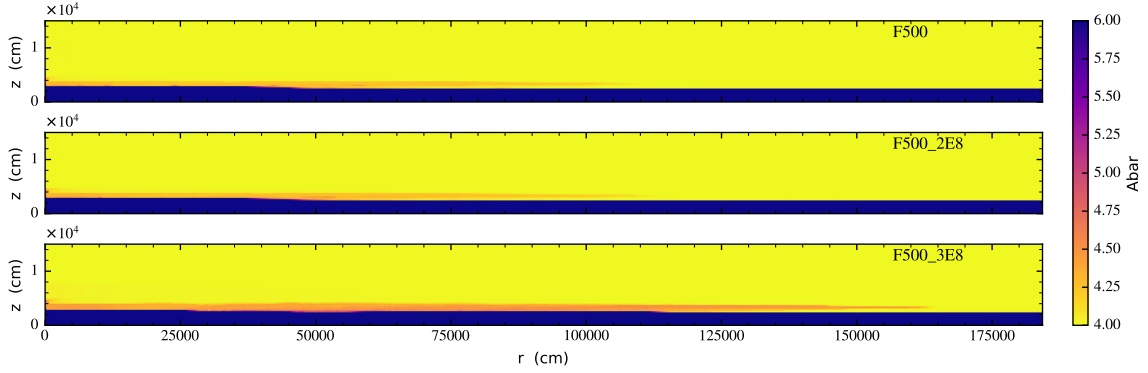


Figure 11. Comparison of \bar{A} for 3 different 500 Hz models with different neutron star temperatures, T_{\star} , and resulting envelope structures. Each flame is shown at 70 ms.

at early times. This disparity may be a direct result of the difference in Coriolis force. It could also be due to the 500 Hz flame taking more time to develop fully and reach higher burning rates, resulting in an $\dot{\epsilon}$ increase over time.

3.3. Effect of Temperature on Flame Structure

To explore the effect of different initial temperature configurations, we run four simulations fixed at a rotation rate of 500 Hz with temperatures as shown in Table 1. For all the 500 Hz simulations (with the exception of the coolest run, F500), we set $T_{\text{star}} = T_{\text{hi}}$, scaling δT accordingly to maintain a consistent value of $T_{\text{hi}} + \delta T$. If we let $T_{\text{star}} < T_{\text{hi}}$, the cooler neutron star surface might act as a heat sink and siphon away energy that would otherwise go into heating the burning layer. By choosing $T_{\text{star}} = T_{\text{hi}}$, we can effectively explore simulations with greater surface heating. There are two physically distinct mechanisms that could each produce an increased temperature at the crust: crustal heating or a higher accretion rate. In these simulations, we cannot distinguish between whether we are generating heat due to a higher accretion rate or due to a shallow crustal heating mechanism, because we are not resolving the crust. Instead, we are modeling the resulting heating effect.

Figure 11 shows \bar{A} for three 500 Hz simulations with different initial temperature structures at $t = 70$ ms. The hottest of the three models, F500_3E8, has a faster propagating flame (discussed further in Section 3.4). It also appears to have a secondary burning region (colored light orange) forming on the far left above the flame edge. It is likely that a small amount of hot material broke out of the flame and rose through the atmosphere. This effect, however, may be numerical rather than physical, resulting from the boundary conditions imposed at the axis of symmetry for these simulations.

Similar to the \bar{A} trends found for different rotation rates in Figure 9, the \bar{A} - T phase plot in Figure 12 suggests that the actual reactions happening in the hottest run may be different than for the cooler runs. Not only is the F500_3E8 flame itself significantly hotter overall, but there is a large causally connected region across a wide range of \bar{A} . This indicates that the hotter temperature has facilitated significant burning in reaction pathways that were not favored at the lower temperatures. The reaction pathways are also very disrupted for F500_3E8 compared to the cooler runs, suggesting that the hotter temperature leads to more turbulent mixing. Compared to the highest rotation rate run, F1000, F500_3E8 reaches a peak temperature roughly 1×10^9 K higher ($\sim 2.7 \times 10^9$ K versus $\sim 1.7 \times 10^9$ K). Though increasing the rotation rate

This is speculation on my part – does someone else have clear idea why? Is this supposed to be enucdot???

NF: I think we should plot peak enucdot as a function of time for each run, it would be useful for me to reference it in one of the later sections

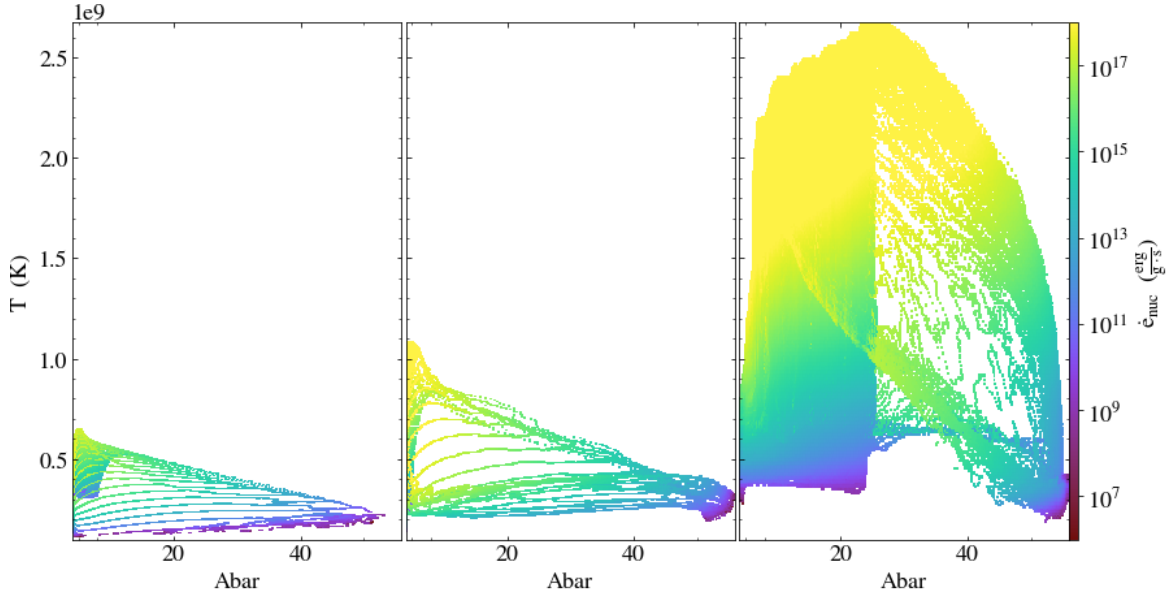


Figure 12. Phase plot of the mean molecular weight \bar{A} , temperature T and the nuclear energy generation rate $\dot{\epsilon}_{\text{nuc}}$ for the 500 Hz runs with T_{star} of 10^8 K, 2×10^8 K and 3×10^8 K.

does seem to concentrate the burning and increase the peak temperature, it does not reach the same level as directly increasing the temperature.

In contrast to the models with $T_{\text{star}} \leq 3 \times 10^8$ K, F500_4E8 is so hot that the organized flame structure is lost. The fuel layer undergoes stable burning and essentially simmers in place, rather than forming a flame; this effect can occur in nature, for neutron stars with accretion that balances the Eddington luminosity (Fujimoto et al. 1981; Bildsten 1998; Keek et al. 2009). This model burns so strongly that it is only run out to 40 ms. After an initial period of burning moves across the domain, residual burning continues and eventually ignites the entire fuel layer at late times, as shown in Figures 13 and 14 for three snapshots taken in the last ten seconds of the simulation. In Figure 13, $\dot{\epsilon}_{\text{nuc}}$ reaches values of $10^{18} - 10^{20} \text{ erg g}^{-1} \text{ s}^{-1}$ across the domain and at heights up to $\sim 0.5 \times 10^4 \text{ cm}$. There is still significant burning occurring even higher, with $\dot{\epsilon}_{\text{nuc}}$ reaching $\sim 10^{15} \text{ erg g}^{-1} \text{ s}^{-1}$ at heights up to $\sim 0.8 \times 10^4 \text{ cm}$. For comparison, the next hottest run (F500_3E8) only reaches maximum $\dot{\epsilon}_{\text{nuc}}$ values of $10^{18} \text{ erg g}^{-1} \text{ s}^{-1}$ and a maximum height of $\sim 0.5 \times 10^4 \text{ cm}$, even at the latest timesteps ($\sim 70 \text{ ms}$, when the flame is most developed). Significant $\dot{\epsilon}_{\text{nuc}}$ values for F500_3E8 are confined to the flame front, rather than spanning the entire domain. . Figure 14 shows \bar{A} for F500_4E8. Again, burning extends across the domain and high into the atmosphere and fuel layer, lacking the characteristic flame structure shown in \bar{A} plots for the lower temperature 500 Hz runs (see Figure 11). A distinct mass of material - resembling a more dramatic version of that shown in Figure 11 - appears to have broken out of the atmosphere near the axis of symmetry. The atmosphere edge is located at $\sim 1.2 \times 10^4 \text{ cm}$. To reiterate, this may just be a result of the imposed boundary conditions rather than a physical effect. F500_4E8 clearly reaches much higher \bar{A} values across the domain (especially at the latest snapshot, $t = 40 \text{ ms}$) compared to all the other runs described in this paper (see Figures 11, 3, and 4). This is not surprising, since as we have seen through our varied temperature simulations, the burning is very temperature-sensitive.

NF: should I include a plot for this or is it ok to just say it?

3.4. Effect of Temperature on Flame Propagation

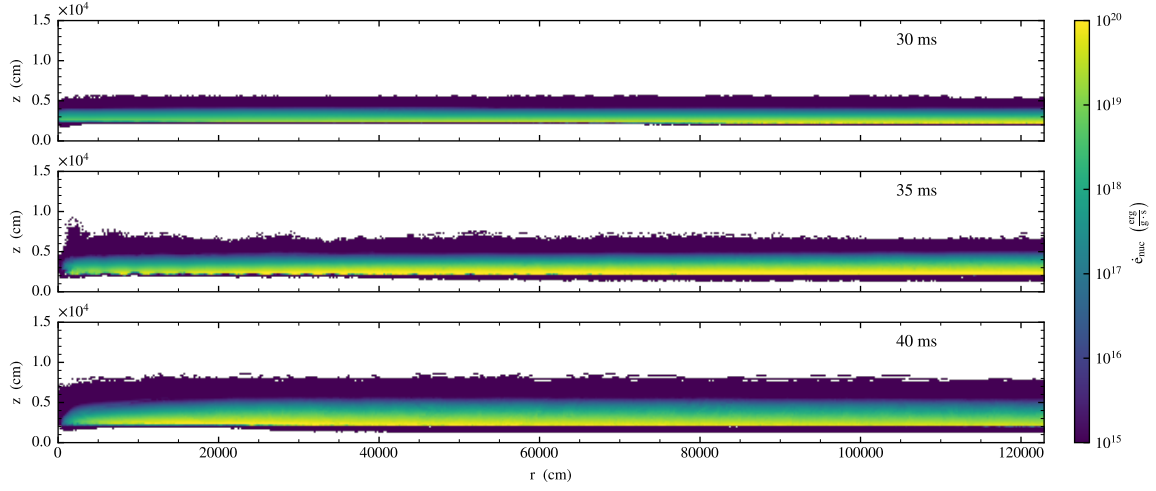


Figure 13. Time series of the 500 Hz run F500_4E8, with $T_{\text{star}} = 4 \times 10^8$ K, showing $\dot{\epsilon}_{\text{nuc}}$. This model burns so strongly that it is only run out to 40 ms; the snapshots shown here are at $T = 30$ ms, 35 ms, and 40 ms.

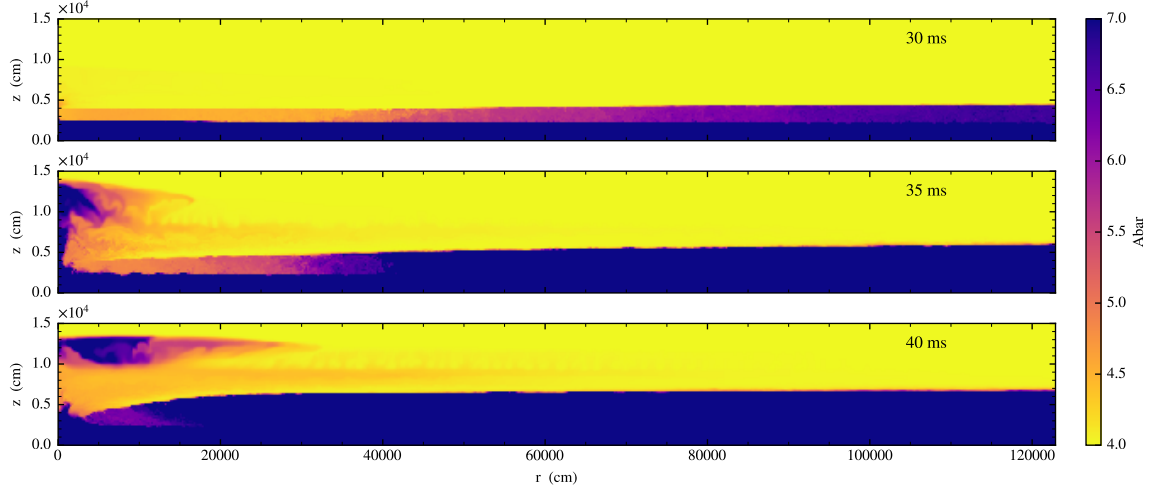


Figure 14. Time series of the 500 Hz run F500_4E8, with $T_{\text{star}} = 4 \times 10^8$ K, showing \bar{A} .

The method for measuring flame propagation described in Section 3.2 is applied in Figure 15 to the three 500 Hz runs with $T_{\text{star}} \leq 3 \times 10^8$ K. Due to the lack of a clear burning front in F500_4E8, we neglect to analyze its propagation speed and acceleration. As the initial T_{star} is increased, the flame becomes greatly accelerated. The initial flame velocities and accelerations derived from a quadratic least-squares fit to each of the datasets are provided in Table 2. The reason for the acceleration of the flame over time is not entirely clear. It could be that energy released from burning begins to dominate the flame's propagation as it evolves, increasing the flame speed over time. Another possibility is that the increased temperatures lead to enhanced

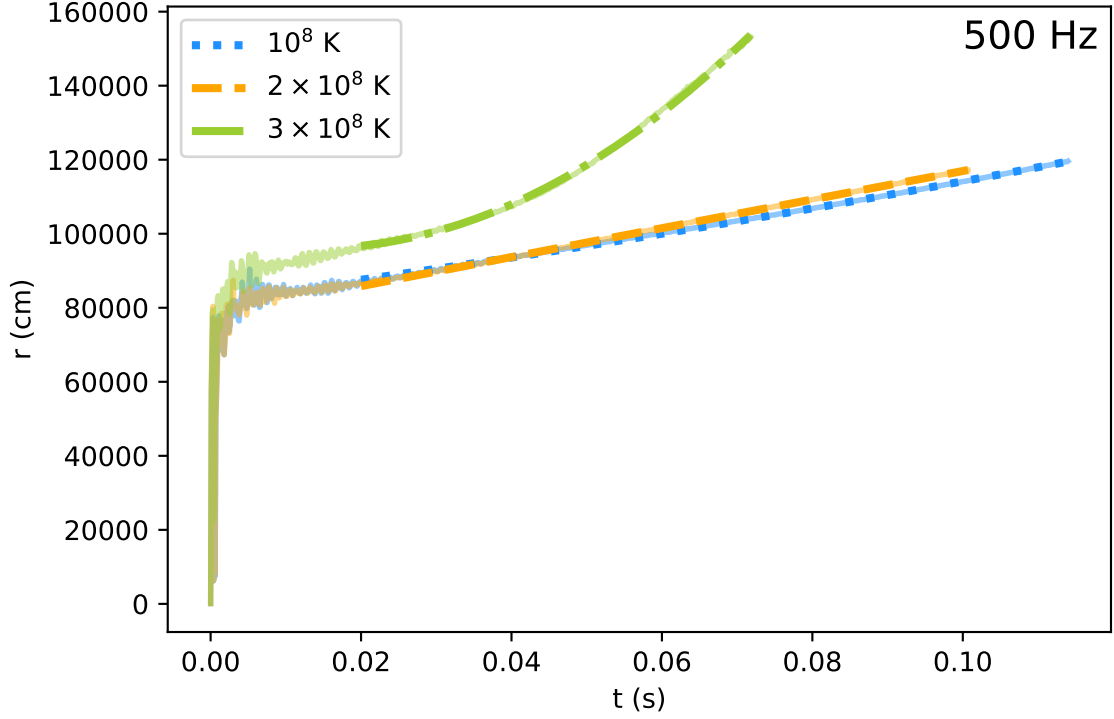


Figure 15. Flame front position vs. time for the three 500 Hz runs with $T_{\text{star}} \leq 3 \times 10^8$ K. The dashed lines show quadratic least-squares fits to the data for $t \gtrsim 0.02$ s. Note that, due to its rapid acceleration, F500_3E8 (orange) is only run out to ~ 0.07 s to avoid surpassing the domain boundary.

turbulent mixing effects that pull in more fresh fuel for the flame to burn. Yet another possibility is that the higher initial T_{star} leads to a greater average temperature in the fuel layer over time, making it easier for the flame to burn the fuel and propagate.

Looking at the phase plots in Figures 16-12, we see:

- The u - ρ plot in Figure 16 shows that the horizontal velocity when $T_{\text{star}} = 3 \times 10^8$ K is sufficiently greater than for the two cooler runs. This is consistent with the plot of the flame front position, where we saw that the hottest flame was significantly faster at later times than the cooler flames.
- The u - v plot in Figure 17 further demonstrates this, as again we see that the magnitude of the velocity of the flame for the hottest run is significantly larger. Also of interest in these plots is that the coolest run does not seem to have developed the characteristic vortex structure at the burning front (i.e. where \dot{e}_{nuc} is greatest) that can be clearly seen for the hotter runs.

4. DISCUSSION AND CONCLUSIONS

tl;dr: faster rotation and/or hotter surface temperature = more burning.

Next steps: tracer particles, 3-d, explore resolution more, H/He flames, MHD flames

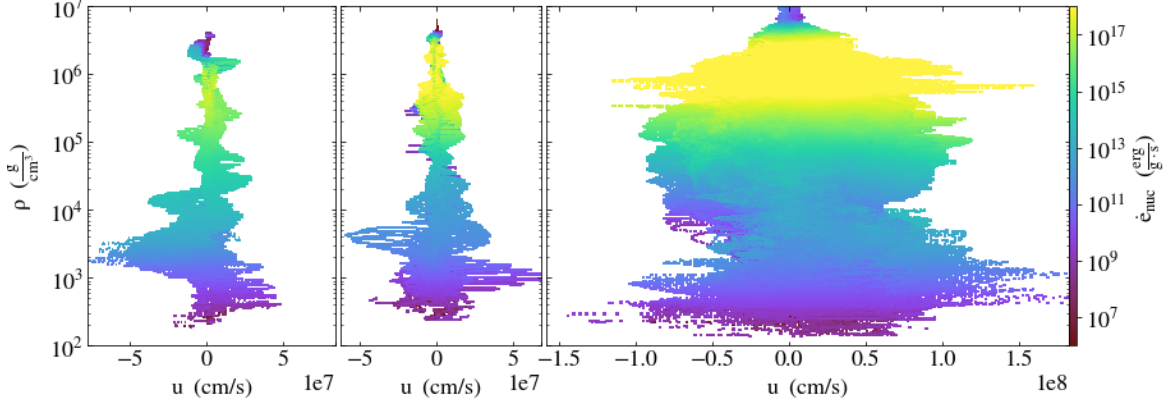


Figure 16. Phase plot of the horizontal x -velocity u , density ρ and the nuclear energy generation rate $\dot{\epsilon}_{\text{nuc}}$ for the 500 Hz runs with T_{star} of 10^8 K, 2×10^8 K and 3×10^8 K.

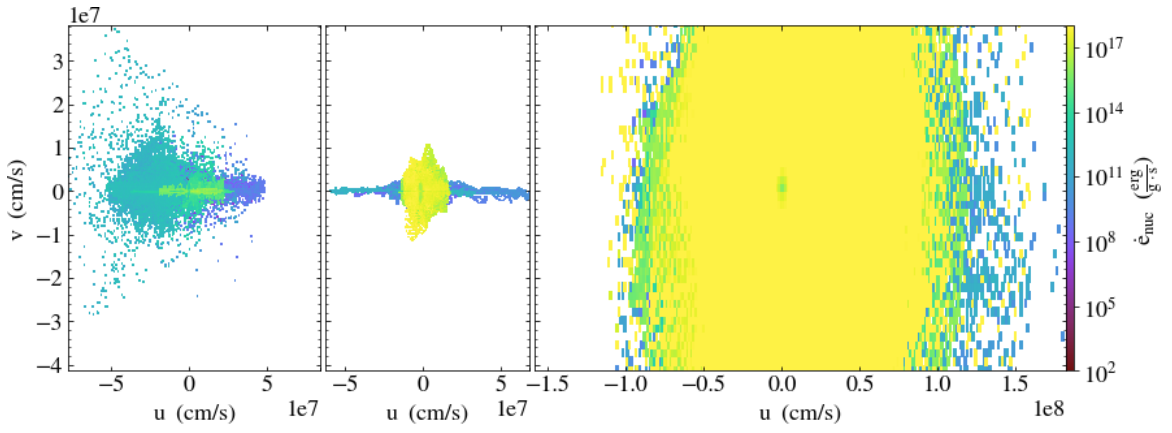


Figure 17. Phase plot of the horizontal x -velocity u , vertical y -velocity v and the nuclear energy generation rate $\dot{\epsilon}_{\text{nuc}}$ for the 500 Hz runs with T_{star} of 10^8 K, 2×10^8 K and 3×10^8 K.

ACKNOWLEDGMENTS

Castro is open-source and freely available at <http://github.com/AMReX-Astro/Castro>. The problem setup used here is available in the git repo as `flame.wave`. The work at Stony Brook was supported by DOE/Office of Nuclear Physics grant DE-FG02-87ER40317. This material is based upon work supported by the U.S. Department of Energy, Office of Science, Office of Advanced Scientific Computing Research and Office of Nuclear Physics, Scientific Discovery through Advanced Computing (SciDAC) program under Award Number DE-SC0017955. This material is also based upon work supported by the U.S. Department of Energy, Office of Science, Office of Advanced Scientific Computing Research, Department of Energy Computational Science Graduate Fellowship under Award Number DE-SC0021110. This work was supported in part by the U.S. Department of Energy, Office of Science, Office of Workforce Development for Teachers and Scientists (WDTs) under the Science Undergraduate Laboratory Internship (SULI) program. MZ acknowledges support from the Simons Foundation. This research used resources of the National Energy Research Scientific Computing Center, a DOE Office of Science User Facility supported by the Office of Science of the U. S. Department of Energy under Contract No. DE-AC02-05CH11231. This research used resources of the Oak Ridge Leadership Computing Facility at the Oak Ridge National Laboratory, which is supported by the Office of Science of the U.S. Department of Energy under Contract No. DE-AC05-00OR22725, awarded through the DOE INCITE program. We thank NVIDIA Corporation for the donation of a Titan X and Titan V GPU through their academic grant program. This research has made use of NASA’s Astrophysics Data System Bibliographic Services.

Facilities: NERSC, OLCF

Software: AMReX (Zhang et al. 2019), Castro (Almgren et al. 2010), GCC (<https://gcc.gnu.org/>), Jupyter (Kluyver et al. 2016), linux (<https://www.kernel.org/>), matplotlib (Hunter 2007, <http://matplotlib.org/>), NumPy (Oliphant 2007; van der Walt et al. 2011), python (<https://www.python.org/>), valgrind (Nethercote & Seward 2007), VODE (Brown et al. 1989), yt (Turk et al. 2011)

REFERENCES

- | | |
|--|---|
| <p>Almgren, A., Sazo, M. B., Bell, J., et al. 2020, Journal of Open Source Software, 5, 2513, doi: 10.21105/joss.02513</p> <p>Almgren, A. S., Beckner, V. E., Bell, J. B., et al. 2010, ApJ, 715, 1221, doi: 10.1088/0004-637X/715/2/1221</p> <p>Altamirano, D., Watts, A., Kalamkar, M., et al. 2010, ATel, 2932, 1</p> <p>Bernard-Champmartin, A., Braeunig, J.-P., & Ghidaglia, J.-M. 2012, Computers and Fluids, 7, doi: 10.1016/j.compfluid.2012.09.014</p> <p>Bhattacharyya, S., & Strohmayer, T. E. 2007, 666, L85, doi: 10.1086/521790</p> <p>Bildsten, L. 1998, in ASIC, Vol. 515, 419</p> <p>Bilous, A. V., & Watts, A. L. 2019, 245, 19, doi: 10.3847/1538-4365/ab2fe1</p> | <p>Brown, P. N., Byrne, G. D., & Hindmarsh, A. C. 1989, SIAM J. Sci. Stat. Comput., 10, 1038</p> <p>Cavecchi, Y., Watts, A. L., Braithwaite, J., & Levin, Y. 2013, MNRAS, 434, 3526, doi: 10.1093/mnras/stt1273</p> <p>Cavecchi, Y., Watts, A. L., Levin, Y., & Braithwaite, J. 2015, MNRAS, 448, 445, doi: 10.1093/mnras/stu2764</p> <p>Chakraborty, M., & Bhattacharyya, S. 2014, ApJ, 792, 4, doi: 10.1088/0004-637X/792/1/4</p> <p>Cumming, A., Macbeth, J., Zand, J. J. M. i. T., & Page, D. 2006, The Astrophysical Journal, 646, 429, doi: 10.1086/504698</p> <p>Deibel, A., Cumming, A., Brown, E. F., & Page, D. 2015, ApJL, 809, L31, doi: 10.1088/2041-8205/809/2/L31</p> |
|--|---|

- Eiden, K., Zingale, M., Harpole, A., et al. 2020, ApJ, 894, 6, doi: [10.3847/1538-4357/ab80bc](https://doi.org/10.3847/1538-4357/ab80bc)
- Fujimoto, M. Y., Hanawa, T., & Miyaji, S. 1981, *Astrophysical Journal*, 247, 267, doi: [10.1086/159034](https://doi.org/10.1086/159034)
- Galloway, D. K., in 't Zand, J. J. M., Chenevez, J., et al. 2020, arXiv e-prints, arXiv:2003.00685. <https://arxiv.org/abs/2003.00685>
- Hunter, J. D. 2007, *Computing in Science and Engg.*, 9, 90, doi: [10.1109/MCSE.2007.55](https://doi.org/10.1109/MCSE.2007.55)
- Johnston, Z., Heger, A., & Galloway, D. K. 2019, arXiv e-prints, arXiv:1909.07977. <https://arxiv.org/abs/1909.07977>
- Katz, M. P., Almgren, A., Sazo, M. B., et al. 2020, in *Proceedings of the International Conference for High Performance Computing, Networking, Storage and Analysis, SC '20* (IEEE Press)
- Keek, L., & Heger, A. 2017, *The Astrophysical Journal*, 842, 113, doi: [10.3847/1538-4357/aa7748](https://doi.org/10.3847/1538-4357/aa7748)
- Keek, L., Langer, N., et al. 2009, *Astronomy & Astrophysics*, 502, 871
- Kluyver, T., Ragan-Kelley, B., Pérez, F., et al. 2016, in *Positioning and Power in Academic Publishing: Players, Agents and Agendas*, 87–90, doi: [10.3233/978-1-61499-649-1-87](https://doi.org/10.3233/978-1-61499-649-1-87)
- Nethercote, N., & Seward, J. 2007, in *Proceedings of the 28th ACM SIGPLAN Conference on Programming Language Design and Implementation, PLDI '07* (New York, NY, USA: ACM), 89–100, doi: [10.1145/1250734.1250746](https://doi.org/10.1145/1250734.1250746)
- Oliphant, T. E. 2007, *Computing in Science and Engg.*, 9, 10, doi: [10.1109/MCSE.2007.58](https://doi.org/10.1109/MCSE.2007.58)
- Spitkovsky, A., Levin, Y., & Ushomirsky, G. 2002, *ApJ*, 566, 1018, doi: [10.1086/338040](https://doi.org/10.1086/338040)
- Timmes, F. X. 2000, *ApJ*, 528, 913, doi: [10.1086/308203](https://doi.org/10.1086/308203)
- Turk, M. J., Smith, B. D., Oishi, J. S., et al. 2011, *ApJS*, 192, 9, doi: [10.1088/0067-0049/192/1/9](https://doi.org/10.1088/0067-0049/192/1/9)
- Turlione, A., Aguilera, D. N., & Pons, J. A. 2015, *Astronomy and Astrophysics*, 577, doi: [10.1051/0004-6361/201322690](https://doi.org/10.1051/0004-6361/201322690)
- van der Walt, S., Colbert, S. C., & Varoquaux, G. 2011, *Computing in Science & Engineering*, 13, 22, doi: [10.1109/MCSE.2011.37](https://doi.org/10.1109/MCSE.2011.37)
- Zhang, W., Almgren, A., Beckner, V., et al. 2019, *Journal of Open Source Software*, 4, 1370, doi: [10.21105/joss.01370](https://doi.org/10.21105/joss.01370)